Integration Of Solution-Processed $BaTiO_3$ Thin Films with High Pockels Coefficient on Photonic Platforms

Ewout Picavet Enes Lievens Kobe De Geest Hannes Rijckaert Edgar Gutierrez Fernandez Oier Bikondoa Eduardo Solano Petriina Paturi Nishant Singh Tinus Pannier Jiayi Liu Xin Yin Dries Van Thourhout Jeroen Beeckman Klaartje De Buysser**

Ewout Picavet, Dr. Hannes Rijckaert, Prof. Dr. Klaartje De Buysser
SCRiPTS, Dept. of Chemistry, Ghent University, Krijgslaan 281-S3, 9000, Ghent, Belgium
Email Adress: klaartje.debuysser@ugent.be
Enes Lievens, Kobe De Geest, Jiayi Liu, Prof. Dr. ir. Jeroen Beeckman
LCP group, Dept. of Electronics and Information Systems, Ghent University, Technologiepark - Zwijnaarde 126, 9052, Gent, Belgium
Email Adress: jeroen.beeckman@ugent.be
Edgar Gutierrez Fernandez, Oier Bikondoa
XMaS, The UK CRG Beamline, European Synchrotron Radiation Facility (ESRF), 71 Avenue des Martyrs, 38043 Grenoble, France
Eduardo Solano
NCD-SWEET beamline, ALBA Synchrotron Light Source, Carrer de la Llum 2-26, 08290, Cerdanyola del Vallès, Spain
Petriina Paturi
University of Turku, Wihuri Physical Laboratory, Dept. of Physics and Astronomy, Vesilinnantie 5, 20014, Turku, Finland
Dr. Nishant Singh, Tinus Pannier, Prof. Dr. ir. Xin Yin
IDLab, Dept. of Information Technology, Ghent University - imec, Technologiepark - Zwijnaarde 126, 9052, Ghent, Belgium
Dries Van Thourhout
Dept. of Information Technology, Ghent University - imec, Technologiepark - Zwijnaarde 126, 9052, Ghent, Belgium

Keywords: *$La_2O_2CO_3$ template film, Ferroelectric $BaTiO_3$ film, Fiber textured films, Pockels effect, Heterogeneously integrated optical phase modulator, Chemical solution deposition*

The heterogeneous integration of ferroelectric $BaTiO_3$ thin films on silicon (Si) and silicon nitride (SiN)-based platforms for photonic integrated circuits (PICs) plays a crucial role in the development of future nanophotonic thin film modulators. Since the electro-optic (EO) properties of ferroelectric thin films strongly depend on their crystal phase and texture, the integration of $BaTiO_3$ thin films on these platforms is far from trivial. So far, a conventional integration route using a $SrTiO_3$ template film in combination with high vacuum deposition methods has been developed, but it has a low throughput, is expensive and requires monocrystalline substrates. To close this gap, a cost-efficient, high-throughput and scalable method for integrating highly textured $BaTiO_3$ films is needed. Therefore, an alternative method for the integration of highly textured $BaTiO_3$ films using a $La_2O_2CO_3$ template film in combination with a chemical solution deposition (CSD) process is presented. In this work, the structural and EO properties of the solution-processed $BaTiO_3$ film are characterized and its integration into an optical ring resonator is evaluated. The $BaTiO_3$ film exhibits a fiber texture, has a large Pockels coefficient (r_{eff}) of 139 pm V^{-1}, and integration into a ring resonator-based modulator shows a $V_\pi L$ of 1.881 V cm and a bandwidth of > 40 GHz. This enables low-cost, high-throughput and flexible integration of $BaTiO_3$ films on PIC platforms and potential large-scale fabrication of nanophotonic $BaTiO_3$ thin-film modulators.

1 Introduction

The excellent functional properties of many perovskite materials have driven the development of heterogeneous integration routes for such materials on silicon (Si) and silicon nitride (SiN)-based platforms for photonic integrated circuits (PICs) to realize a variety of novel photonic devices.[1, 2, 3] One of the most important building blocks for these photonic devices is the nanophotonic phase modulator, for which ferroelectric materials like $LiNbO_3$,[4, 5] $Pb(Zr,Ti)O_3$,[6, 7] $BaTiO_3$[8, 9] are integrated on these PIC platforms to combine the advantages of their excellent electro-optic (EO) properties with the low manufacturing costs of integrated silicon photonics (SiPh). This opens up a way to produce pure EO phase shifters based

on the linear EO effect (Pockels effect) with high linearity, high efficiency, low optical losses and no unwanted residual amplitude modulation. A simplified description of the Pockels effect is given by a linear relationship between the change in refractive index ($\Delta n(E)$) due to an applied external electric field (E) according to the following equation:

$$\Delta n(E) = -\frac{1}{2} r_{eff} n_0^3 E \quad (1)$$

In this equation, r_{eff} (pm V^{-1}) is the effective Pockels coefficient, n_0 is the refractive index in the absence of an electric field and E (V cm^{-1}) is the applied electric field. Among ferroelectric materials, $BaTiO_3$ is considered one of the most promising future materials for three reasons. First, it has one of the largest Pockels coefficients of all EO materials.[10, 11, 12] Second, it is a lead-free material. Third, it is a chemically and thermally stable metal oxide material. Over the years, this has led to the development of high-speed $BaTiO_3$ film modulators with low propagation loss,[13] high-speed modulation,[14, 15] and low power consumption,[16] confirming the great potential of heterogeneous integrated $BaTiO_3$ thin film modulators on PIC platforms.

Despite their outstanding performance, the integration of highly textured $BaTiO_3$ films on PIC platforms is anything but trivial. Since the EO properties of $BaTiO_3$ films strongly depend on their crystal phase and film texture, an epitaxial integration process was developed to obtain highly textured $BaTiO_3$ films.[17, 18, 19, 20] Traditionally, a $SrTiO_3$ template film is epitaxially grown on monocrystalline Si, which facilitates the epitaxial integration of a $BaTiO_3$ film on the $SrTiO_3$ film due to the high lattice match between the $SrTiO_3$ material (a: 3.905 Å) and the $BaTiO_3$ material (a: 3.994 Å, c: 4.0335 Å) .[21, 22] Subsequently, the deposition of a highly textured $BaTiO_3$ film is usually carried out by high-vacuum techniques such as molecular beam epitaxy (MBE),[23, 24, 25] pulsed laser deposition (PLD),[24, 26] and RF sputtering.[
Once an epitaxial $BaTiO_3$ film is formed, the film can be integrated by integration methods such as direct wafer bonding, transfer printing and flip-chip on non-monocrystalline Si substrates.[15, 9] Although integration is feasible, this conventional route has several disadvantages. First, the $SrTiO_3$ template film has been shown to be an important source of propagation loss.[13] Second, the use of high vacuum methods appears to be necessary to fabricate highly textured $BaTiO_3$ films with a strong (Pockels) effect[12, 28, 29] or $BaTiO_3$ metasurfaces must be fabricated for nonlinear EO effects.[30, 31, 32] Third, the $BaTiO_3$ film formation must be carried out on a monocrystalline Si substrate, which drastically limits the flexibility of integration. All this limits the fabrication and integration of $BaTiO_3$ thin films into nanophotonic thin film modulators on a large scale. Therefore, there is a need for a low-cost, high-throughput and more flexible integration method to pave the way for large-scale integration of $BaTiO_3$ films on PIC platforms.
Here, we propose such an alternative processing route based on two fundamental changes: the use of a $La_2O_2CO_3$ template film and the integration of $BaTiO_3$ thin films via a chemical solution deposition (CSD) process. The $La_2O_2CO_3$ template film exhibits low losses and inherent self-orientation behavior that ensures compatibility with various substrates and allows both *in situ* processing routes (direct integration) on photonic platforms that can withstand the higher annealing required to integrate both films, as well as *ex situ* processing routes (integration via bonding methods) when *in situ* processing is not possible due to the thermal budget of the processed platform.[6, 33] In this way, the flexibility of integration and/or compatibility with the thermal budget can be achieved during the different processing phases of the photonic platforms. In addition, integration via solution processing offers a route to a cost-effective and high-throughput process.
In this work, the solution-processed $BaTiO_3$ stack was first structurally characterized to investigate its crystal phase, film texture and surface roughness. Then, the EO properties were evaluated and the $BaTiO_3$ film was integrated into a SiN O-band ring resonator to evaluate and validate the proposed solution process as an integration route to fabricate a high-speed thin film modulator. The $BaTiO_3$ film exhibits a tetragonal phase (P4mm) and is fiber textured with the longer c-axis randomly aligned in-plane, as well as a characteristic microstructure and low surface roughness. This highly textured film yields a large r_{eff}, high modulation efficiency and large bandwidth of the SiN O-band ring resonator. In summary, this solution process provides a low-cost, high-throughput and flexible integration route for $BaTiO_3$ films on

photonic platforms, which can enable the large-scale fabrication of new nanophotonic thin film modulators.

2 Results and discussion

2.1 Microstructural characterization of the solution processed $BaTiO_3$ film

Since the EO properties of the $BaTiO_3$ film are closely related to its crystal phase and film texture, these structural properties of the integrated $BaTiO_3$ film are evaluated first. In Figure 1a the formed $BaTiO_3$ phase is evaluated by comparing the azimuthal integration of the 2D grazing incident wide-angle X-ray scattering (GIWAXS) recorded images of the $BaTiO_3$ film with a powder diffraction file (PDF) of the ferroelectric tetragonal $BaTiO_3$ crystal phase (P4mm). Here, all reflections show high agreement with the PDF file (PDF: 00-05-0626), without the presence of additional secondary phases. The tetragonal crystal phase is clearly recognisable by the peak splitting of the (002)/(200) reflection (see inset figure), which is due to the elongated c-axis lattice parameter.
In addition to the formation of the desired ferroelectric crystal phase, the $BaTiO_3$ films also exhibit a high degree of texture. In Figure 1b, out-of-plane θ-2θ X-ray diffraction (XRD) measurements of the $BaTiO_3$ film integrated on different substrates (Si, Si/SiO_2, Si/SiN, corning glass (CG) and CG/ITO) show only strong (h00) reflections. Consequently, the $BaTiO_3$ film exhibits a preferred (h00) out-of-plane orientation which is not influenced by the nature of the substrate. This preferential orientation is caused by the $La_2O_2CO_3$ template film, which acts as a self-orienting template film compatible with both crystalline and amorphous substrates [33]. The preferred out-of-plane orientation of the $BaTiO_3$ film is quantitatively expressed by a calculated Lotegeringsfactor (LF) of 0.978 (see experimental section). Although the LF value is close to 1, the $BaTiO_3$ films also contain a small volume fraction of randomly oriented regions, since traces of the (110) and (111) planes are also present in the θ-2θ XRD measurements. In addition, the crystallite size (D) and microstrain ($\mu\epsilon$) were also calculated using the Williamson-Hall method for all $BaTiO_3$ films on the different substrates (Si, Si/SiO_2, Si/SiN, CG and CG/ITO).[34, 35] This results in an average D of 66.68 ± 2.47 nm and $\mu\epsilon$ of 3.23 ± 0.16, whereby the error represents a standard deviation. The low standard deviation confirms the fact that the type of substrate has almost no influence on the $BaTiO_3$ film formation. For further evaluation of the $BaTiO_3$ film texture, both out-of-plane and in-plane θ-2θ for a narrower interval of 2θ (43°-47°) are shown in Figure 1c. Here it becomes clear that the a-axis (200) - ($2\theta = 45.411°$) - is out-of-plane oriented while the elongated c-axis (002) - ($2\theta = 44.972°$) - is in-plane oriented. Therefore, we will refer to these $BaTiO_3$ films as a-axis oriented, since the shorter a-axis is oriented out-of-plane [12]. Subsequently, the lattice parameters of the $BaTiO_3$ film (a = 3.99(1) Å, c = 4.02(8) Å, c/a = 1.00(9)) can be calculated from both reflections. These show good agreement with the lattice parameters of the ferroelectric bulk $BaTiO_3$ (PDF:00-05-0626) (a = 3.994 Å, c = 4.038 Å, c/a = 1.011). Most likely, the preferred orientation of the longer c-axis (4.02(8) Å) in-plane is related to the attempt to match the even larger $La_2O_2CO_3$ template film lattice parameter (4.076 Å). However, it should be noted that the in-plane lattice parameter c given here should be considered as an approximation due to crystal lattice distortions (e.g. strain, defects, etc.) and the possible coexistence of small c-axis oriented volume fractions in the film. Furthermore, it was investigated whether this preferred orientation of the a-axis is maintained after multiple $BaTiO_3$ depositions, since in the conventional method with the $SrTiO_3$ template film, the $BaTiO_3$ film thickness often influences the preferred orientation of the elongated c-axis.[36, 25] This is related to the smaller $SrTiO_3$ lattice parameter (3.905 Å) which induces c-axis orientation for thin films (<50 nm) which relaxes to a-axis orientation for thicker films (> 50 nm). Figure S1 shows out-of-plane and in-plane θ-2θ for single-deposited (65 nm) and triple-deposited (190 nm) thick $BaTiO_3$ films. These results prove that the preferred orientation of the a-axis orientation is maintained and is not affected by the $BaTiO_3$ film thickness.
To evaluate the in-plane orientation of the film, a pole figure measurement of the (101) plane at $2\theta = 31.507°$ of the $BaTiO_3$ film was performed and plotted in Figure 1d. Here, a ring at $\chi = 45°$ is observed indicating that there is no preferred in-plane orientation, which is consistent with the corresponding fiber

texture orientation of the $La_2O_2CO_3$ template film. [33] In other words, the $BaTiO_3$ film can be integrated on different substrates and has a fiber texture with its elongated c-axis randomly oriented in-plane. Since the elongated c-axis is also the polar axis of the film, the polar axis of a $BaTiO_3$ unit cell is randomly oriented in-plane, as graphically illustrated and shown in Figure 1e. Consequently, this leads to the formation of randomly in-plane oriented polarization domains, which is in stark contrast to the traditionally epitaxial integrated $BaTiO_3$ films where only 90° and 180° domains walls are present due to the use of an epitaxial $SrTiO_3$ template film.[37, 38, 39, 40]

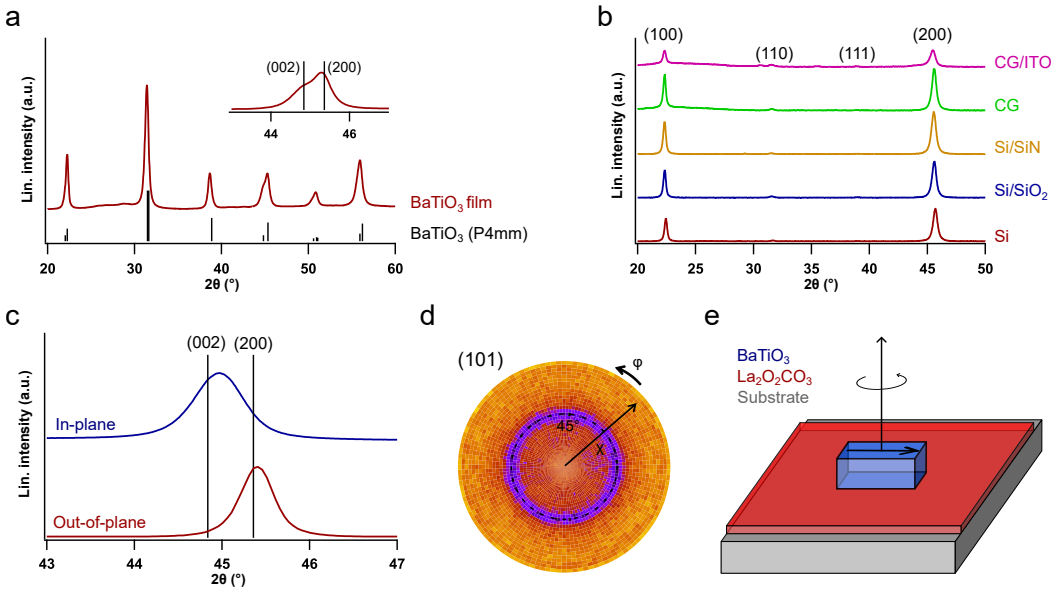

Figure 1: (a) The azimuthally integrated GIWAXS data of the $BaTiO_3$ film is compared with the tetragonal ferroelectric $BaTiO_3$ phase (PDF: 00-05-0626). The tetragonal crystal phase of the $BaTiO_3$ film is clearly observed in the peak splitting of the (002)/(200) reflection (see inset figure). (b) Out-of-plane θ-2θ XRD measurements of integrated $BaTiO_3$ films on different substrates. A film with strong out-of-plane (h00) preferential orientation is present on all substrates. (c) The $BaTiO_3$ film preferentially orients its elongated c-axis in-plane. (d) No preferred in-plane orientation is present as a circle is present in the pole figure measurement of the (101) plane. (e) Illustration of the fiber texture present in the solution processed $BaTiO_3$ film which causes the random orientation of the elongated c-axis (polar axis) in-plane.

In addition to the structural characterization by X-ray diffraction, the highly textured $BaTiO_3$ film is also visualized by high-resolution transmission electron microscopy (HRTEM), as shown in Figure 2a,b. Here, the integration of a highly crystalline $BaTiO_3$ film on a Si/SiO_2 substrate using the $La_2O_2CO_3$ template film is confirmed. The observed large interference patterns in the HRTEM image (Figure 2a) are Moiré fringes.[41, 42, 43] On the high magnification image (Figure 2b), the preferential out-of-plane orientation of the $BaTiO_3$ film is clearly visible and is also confirmed by the fast Fourier transform (FFT) analysis (see inset figure). To determine whether Si diffusion is present in the $BaTiO_3$ film, the compositional gradient of the entire stack is examined by X-ray photoelectron spectroscopy (XPS) depth analysis (Figure S2). Here, the representative elements (Ba, Ti, O) are homogeneously distributed in the $BaTiO_3$ film, with the Ba/Ti ratio close to 1. The compositional anomaly of the surface signal is related to the sensitivity of the $BaTiO_3$ films to surface contamination under ambient conditions.[44, 45] Consequently, there is no evidence of Si diffusion in the $BaTiO_3$ film, confirming that the $La_2O_2CO_3$ template film also acts as an efficient diffusion barrier.

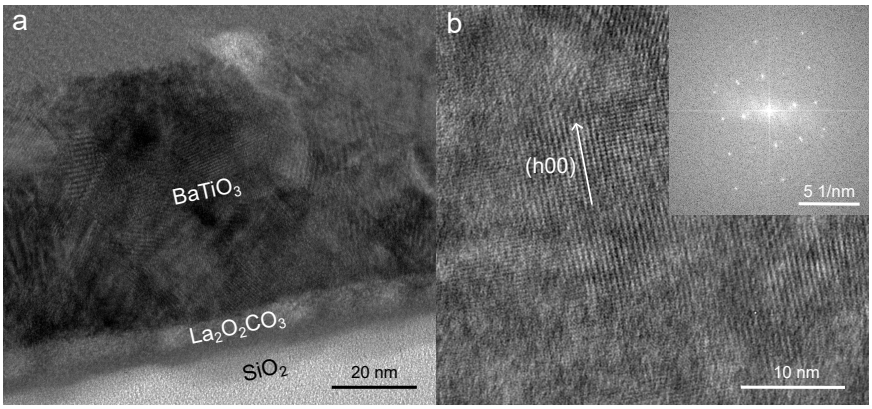

Figure 2: (a) HRTEM image of a $La_2O_2CO_3/BaTiO_3$ stack integrated on a Si/SiO_2 substrate showing a highly crystalline $BaTiO_3$ thin film. (b) HRTEM image and FFT analysis of the $BaTiO_3$ film showing the preferred out-of-plane orientation of the $BaTiO_3$ thin film.

In addition to the structural properties, low surface roughness is also an important prerequisite for the $BaTiO_3$ films as this can contribute significantly to the propagation losses by acting as a source of scattering.[46] Figure 3a,b shows planar-view scanning electron microscopy (SEM) of the $BaTiO_3$ film. The surface morphology of the films is dense and smooth and has a grain-like microstructure. Interconnected grains with a diameter of 10-80 nm are observed which is in accordance with the earlier determined crystallite size calculated via XRD. Some pores of varying depths can be observed throughout the film, but these are limited to 5-30 nm (see inset figure).[47] The roughness of the $BaTiO_3$ film was quantified by surface analysis using atomic force microscopy (AFM) (Figure 3b) and yielded a low root mean square (RMS) roughness value of 2.51 nm for a 65 nm thick $BaTiO_3$ film. This value is lower or comparable to other processed $BaTiO_3$ films.[48, 49, 50, 51]

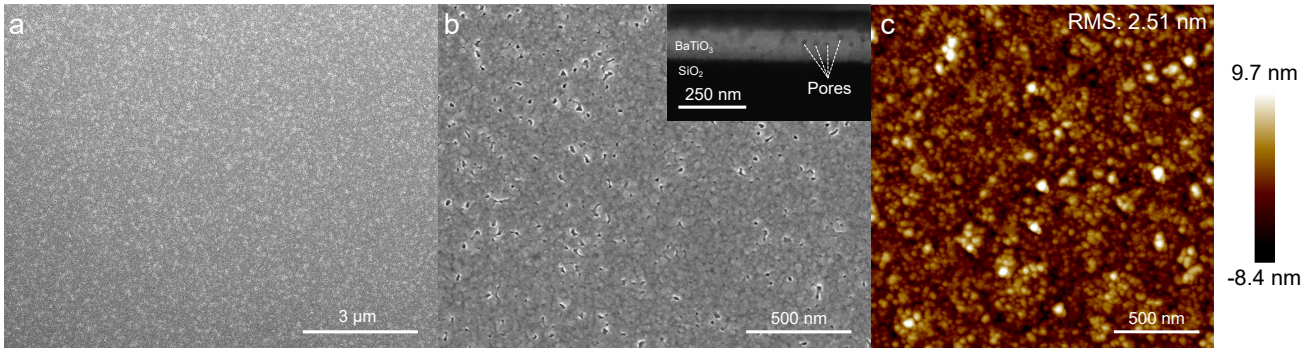

Figure 3: Surface analysis by SEM and AFM shows that the ferroelectric stack has (a,b) a dense microstructure with some small pores (b) a low surface roughness (RMS of 2.51 nm) for a 65 nm thick $BaTiO_3$ film.

2.2 Determination of the Pockels coefficient of the $BaTiO_3$ film

Before we integrate our fiber textured $BaTiO_3$ films on PICs, it is important to evaluate their properties under optical and electric fields. Before the EO measurements, we first determined the dielectric constant and the loss tangent of the film (Figure S3 and S4). This results in an in-plane dielectric constant of 3660 and a loss tangent of 0.07. EO measurements are then carried out and the Pockels coefficient is calculated using equation (6) in the experimental section. Since the optical power is mapped linearly to a voltage through the photodetector, the equation (6) can be expressed in the form of the photodetector voltage V_{PD}. If we now consider the change in the photodetector voltage due to a modulation voltage (i.e. we take the derivative after the modulation voltage V_{mod}), we obtain the following expression (see SI, equation (S11)):

$$r_{eff} = \frac{\lambda g}{\alpha n^3 \pi t V_{PD,0}} \frac{\partial V_{PD}}{\partial V_{mod}} \quad (2)$$

Where λ (1550 nm) is the wavelength of the laser, g (10 μm) is the distance between the electrodes, α (0.942) is a correction term for the electric field (see experimental section),[52] n (2.1) is the refractive index, t (190 nm) is the thickness of the film (selected to achieve a good signal-to-noise ratio), $V_{PD,0}$ (V) is the photodetector voltage, and $\partial V_{PD}/\partial V_{mod}$ is the change in photodetector voltage due to the modulated signal.

The calculated r_{eff} of the $BaTiO_3$ film as a function of an external DC bias field ($E_{\mathrm{DC}} = V/g$) is shown in Figure 4a (raw data can be found in Figure S5). Initially, the unpoled $BaTiO_3$ film shows almost no EO response because the polarization domains are randomly oriented in-plane and the responses of two antiparallel domains cancel each other out. An increase in E_{DC} leads to a strong increase in r_{eff}, which results from the realignment of the in-plane polarization domains, eliminating antiparallel domains. Finally, all polarization domains are maximally aligned with the applied electric field component and the r_{eff} is saturated. An overview of a possible domain realignment process is shown in Figure 4b. Here, the reorientation is represented by the electric dipole in the unit cell, which can switch its polar axis by 90° (green) or 180° (purple) to maximize the alignment of its electric dipole with the applied field. Since the polar axis is parallel to the elongated axis of the unit cell, the applied E_{DC} also leads to a spatial change of the unit cell and consequently to stress and strain in the $BaTiO_3$ film.[53] Once the sample is fully poled, a symmetrical hysteresis loop is monitored during a full sweep of E_{DC}, which is a clear signature of the ferroelectric nature of the stack.[24, 51] The decreasing slope at large $|E_{DC}|$ values results from nonlinear EO effects.[23] To evaluate the average maximum and remnant response of the $BaTiO_3$ film, different electrode pads were measured and the measurements were performed several times per pad. This resulted in an average maximum r_{eff} of 138.68 $\mp$ 5.78 pm V^{-1} and a remnant r_{eff} coefficient of 26.38 $\mp$ 18.05 pm V^{-1}, whereby the specified error is a standard deviation. The error is due to small variations in processing conditions, including electrode spacing and thickness variations. In addition, a coercive field of $E_c = 0.5$ V μm^{-1} can be derived from the shape of the hysteresis, which is an order of magnitude larger than in bulk $BaTiO_3$. Such an increase is typically observed in ferroelectric thin films due to domain pinning and a finite depolarization field.[54] Furthermore, the stability of the EO response over time was evaluated and shown in Figure 4c. Here, both the remnant r_{eff} ($E_{DC} = 0$ V μm^{-1}) and the maximized r_{eff} ($E_{DC} = 5$ V μm^{-1}) are measured over 40 hours. Apart from small changes in the first hours, which are related to transient phenomena regarding domain reorientation, the EO response is very stable over time.

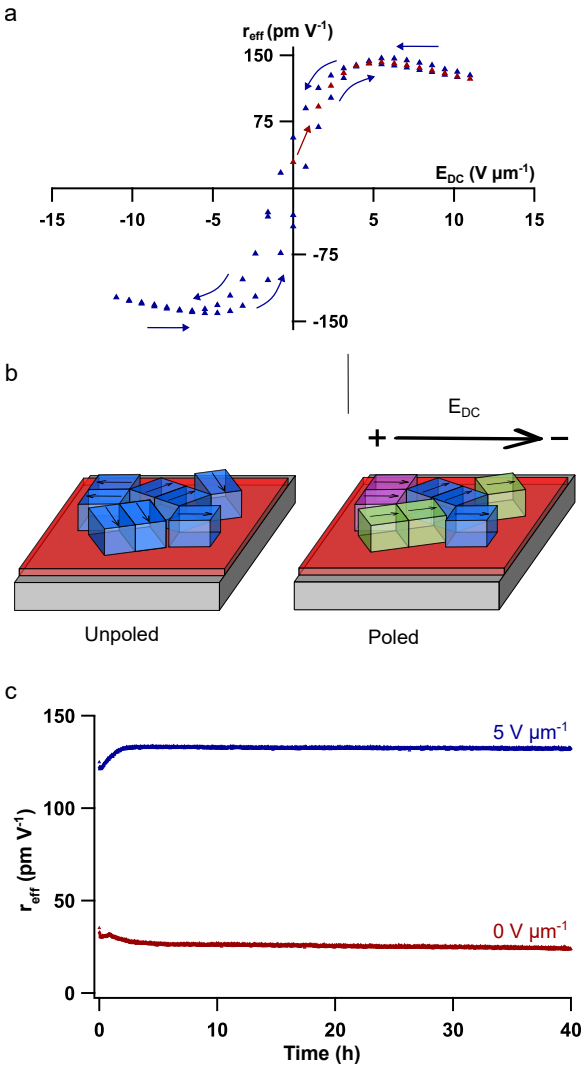

Figure 4: (a) The $BaTiO_3$ exhibits a hysteresis loop after poling, as expected due to the reorientation of the in-plane polarization domains as the field is swept back and forth. (b) Graphical illustration of the reorientation of the electric dipole moment in the unit cell by applying an electric field. The green unit cells have rotated their polar axis 90° while the purple unit cells have rotated their polar axis 180°. (c) A small remnant r_{eff} remains present in the film and is stable over a long time. Also, a high r_{eff} remains present and very stable in the film at $E_{DC} = 5$ V μm^{-1}.

In order to evaluate the r_{eff} value of our solution processed $BaTiO_3$ film, it is compared with the r_{eff} values already reported in the literature, which are shown in Table 1. Only r_{eff} values measured in a transmission geometry, like the one used in this work, are considered here, as other reported r_{eff} values which are measured differently lead to a different definition of r_{eff} and are therefore not directly comparable in all cases. The definition of r_{eff} used to compare between our results and literature is given as:

$$r_{eff} = r_{33} - r_{13} \tag{3}$$

Where r_{33} and r_{13} are components of the Pockels tensor. As previously mentioned, the highest r_{eff} values are traditionally obtained by high vacuum deposition methods, in particular by MBE, with a $SrTiO_3$ template film. To our knowledge, we are the first to propose an alternative solution process that yields a comparable r_{eff} value (Table 1).

The reason for this is most likely twofold. First, the high maximum coefficient r_{eff} obtained in this work is due to the inherent preferential a-axis orientation in the solution-processed $BaTiO_3$ stack, as previous work has shown that the EO response increases significantly with increasing volume fraction of a-axis orientation in the film.[24, 56] The large intrinsic fraction of a-axis orientation in our film is in contrast to traditionally processed $BaTiO_3$ films using a $SrTiO_3$ template film, as the a-axis orientation only becomes dominant after a critical minimum film thickness is exceeded and/or post-annealing processes are

Table 1: Comparison of the measured r_{eff} of integrated $BaTiO_3$ thin films in a transmission geometry set-up. All measurements were performed at a wavelength of 1550 nm.

Method	Substrate/template film	Thickness $BaTiO_3$ (nm)	r_{eff} (pm V^{-1})
MBE [23]	$Si/SrTiO_3$	130	148
MBE [24]	$Si/SrTiO_3$	78	140
CSD (our work)	$Si/SiO_2/La_2O_2CO_3$	190	139
RF sputter [25]	$Si/SrTiO_3$	300	131
CSD [55]	$Si/SrTiO_3$	90	89
MBE [36]	$Si/SrTiO_3$	90	46
RF sputter [24]	$Si/SrTiO_3$	96	41
PLD [24]	$Si/SrTiO_3$	97	37
CVD [24]	$Si/SrTiO_3$	70	7

required, to reverse the c-axis orientation to the desired a-axis orientation in thin $BaTiO_3$ films.[36, 57, 26, 58] Second, due to their random in-plane polarization orientation, almost all the unit cells are able to align their polar axis along the direction of E_{DC} via 90° or 180° domain switching. In other words, each individual polarization domain is able to maximally align their polar axis with the applied electric field component. Furthermore, this random in-plane orientation greatly simplifies the complexity of integrating the electrodes, as they can be integrated in any in-plane orientation and still provide the same EO response.

2.3 Integration of the $BaTiO_3$ film into a SiN ring resonator

To validate the operation in functional devices, a $BaTiO_3$ film is integrated into a SiN O-band ring resonator (see experimental section). In Figure 5a,b. shows the top view of a ring modulator with gold electrode pads and the waveguide cross-section. Since the polarization domains in the $BaTiO_3$ films are randomly oriented in-plane, the distribution of the polarization domains will be uniform along the ring resonator circumference, which means that it is possible to deposit electrodes along its entire circumference. Light with a wavelength centered around 1310 nm is coupled into the fundamental quasi-transverse electric (quasi-TE) optical mode. A simulation of this quasi-TE mode is shown in Figure 5c, which shows that a significant fraction (33%) of the optical mode is confined in the $BaTiO_3$ film. The transmission spectrum of the O-band ring modulator is shown in Figure 5d. Similar to the measurements in free space, an external DC bias field E_{DC} is applied, which causes a refractive index shift in the $BaTiO_3$ film, changing the resonant wavelength of the ring resonator and turning it into a functional EO modulator. In Figure 5e, the shift of the resonance wavelength is plotted as a function of the applied voltage. The tuning efficiency is now calculated as the slope of the wavelength shift due to an applied voltage $\Delta\lambda/\Delta V$, which is shown in Figure 5f. This graph shows a first region with a non-linear trend (below $E_{DC} = 2.3$ V μm^{-1}) and a second region exhibiting a linear trend (R = 0.9991) (above $E_{DC} = 2.3$ V μm^{-1}). This is to be expected as not all polarization domains are already aligned in this first region, resulting in the change in refractive index (equation (1)) being a combination of an increasing r_{eff} and a DC bias. Once a DC bias field of $E_{DC} = 2.3$ V μm^{-1} is reached, all polarization domains are fully aligned and the r_{eff} saturates. Consequently, a linear relationship is observed between the resonance shift and the applied DC voltage. This linear section shows a tuning efficiency of $\Delta\lambda/\Delta V = 18.39$ pm V^{-1}. This tuning efficiency is then used to determine the half-wave voltage-length product, which is defined as follows:

$$V_\pi L = \frac{L\lambda_{FSR}\Delta V}{2\Delta\lambda} \tag{4}$$

Where L (654.50 μm) is the length of the phase shifter, λ_{FSR} (1.057 nm) is the free spectral range and $\Delta\lambda/\Delta V$ (pm/V) is the tuning efficiency of the ring. From the half-wave voltage-length product it is possible to calculate the Pockels coefficient responsible for the phase tuning in the waveguide structure r_{wg}, using equation (5). Note that this is not the same Pockels coefficient as mentioned above, as the align-

ment of the electrical field and polarization of the light is different. Here, the polarization of the light coupled into the waveguide is a TE mode and is parallel to the electric field.

$$r_{wg} = \frac{\lambda g}{\Gamma n^3 V_\pi L} \tag{5}$$

Where λ (1310 nm) is the wavelength, g (6 μm) is the distance between the electrodes, n (2.1) is the refractive index of the $BaTiO_3$ film, Γ (0.4) the electro-optic overlap integral (equation (S1)) and the $V_\pi L$ half-wave voltage-length product of the ring.[6] In order to evaluate the average modulation of the $BaTiO_3$ film, different ring structures were measured and the measurements were performed several times per ring. This resulted in a half-wave voltage-length product of $V_\pi L = 1.881 \mp 0.078$ V cm and $r_{wg} = 111.47 \mp 4.42$ pm V^{-1}, where the specified error is a standard deviation. The error is due to small variations in processing conditions, including electrode spacing and thickness variations. These results are comparable to those reported for state-of-the-art epitaxial $BaTiO_3$ thin films.[23, 25]

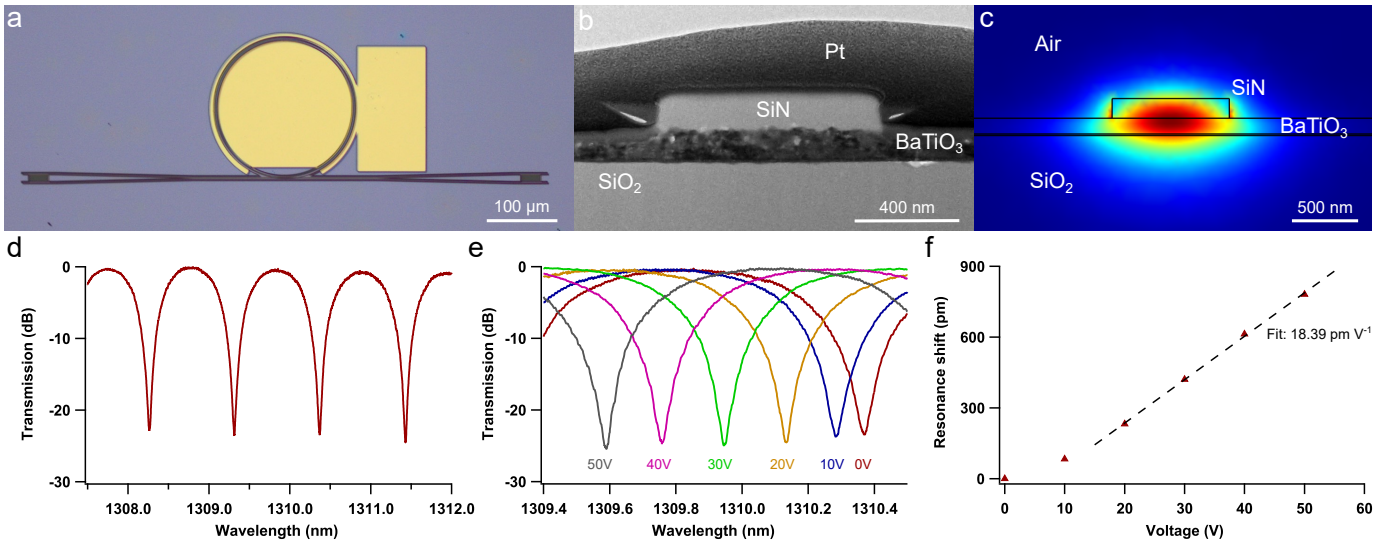

Figure 5: Design and response of a C-band ring modulator. (a) Top view of the SiN waveguides fabricated on the $BaTiO_3$ film. (b) Cross-sectional TEM view of the SiN waveguide on the $BaTiO_3$ film. Note: The $La_2O_2CO_3$ film (7 nm) is not visible at this magnification. (c) Simulation of the TE optical mode in the waveguide structure. (d) Normalized transmission spectrum of the O-band ring modulator with a $\Delta\lambda_{FSR}$ of 1.057 nm (e) The normalized transmission spectra for different DC voltages. (f) The resonance wavelength shift in function of the applied voltage across the $BaTiO_3$ film shows the expected linear trend above a DC voltage of 15 V with a tuning efficiency of 18.39 pm V^{-1}.

To complete the results for the $BaTiO_3$ SiN O-band ring modulator, high-speed measurements of the scattering matrix were performed. The $|S_{21}|$ S-parameter was measured as a function of modulation frequency, as $|S_{21}|$ represents the forward transmission of the device, the results of which are shown in Figure 6. In Figure 6a, $|S_{21}|$ is shown for different DC voltages. Here, a clear increase in forward transmission is observed for higher DC voltages, which can be attributed to the increase in Pockels coefficient in our $BaTiO_3$ film for higher DC voltages (see Figure 4). The increase in forward transmission is linear for small DC voltages and saturates towards higher DC voltages, which is in accordance with the measured Pockels coefficient under DC bias. In Figure 6b, the electro-optic-electro (EOE) and the electro-optic (EO) bandwidths are given for the device under 10V DC bias. First, the EOE bandwidth, which is defined as the 3 dB cut-off, is about 24 GHz. Second, the EO bandwidth, which is defined as the 6 dB cut-off, is approximately 43 GHz. The bandwidths shown here are most likely not limited by the material properties of the fiber textured $BaTiO_3$ film, but by the design of the device, as the Pockels effect is theoretically present up to around $\sim 10^{12}$ Hz, i.e. in the terahertz range. In state-of-the-art EO modulators, bandwidth up to 100 GHz has been reported. Consequently, higher bandwidth can most likely be achieved by optimizing the modulator design for high speed operation.[59, 60, 61]

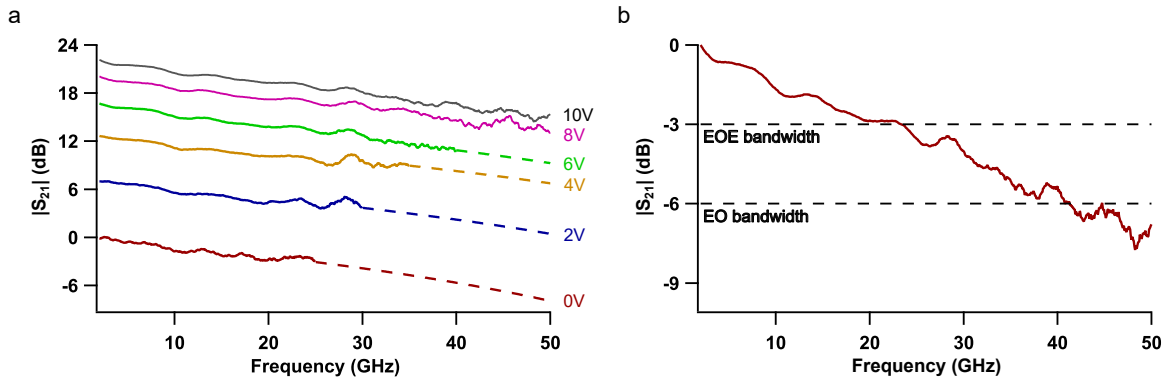

Figure 6: (a) Frequency response of the $|S_{21}|$ S-parameter. The curves were all normalised with respect to unbiased DC operation. An increase in forward transmission is observed since for higher DC bias voltages, a higher Pockels coefficient is observed. The dotted lines represent extrapolated data. (b) Bandwidth of the ring resonator under 10V DC bias. Large EOE (24 GHz) and EO (43 GHz) bandwidths are measured indicating the possibility of high-speed modulation. The device bandwidth gives similar values for each DC bias. Indicating that device bandwidth is independent of modulation strength.

3 Conclusion

In summary, the integration of a solution-processed $BaTiO_3$ film on a PIC platform using the alternative $La_2O_2CO_3$ template film yields a fiber textured ferroelectric $BaTiO_3$ film with its elongated c-axis randomly in-plane oriented. Since the elongated axis is also the polar axis of the film, the polarization domains are randomly oriented in- plane. In addition, the $BaTiO_3$ film has a low surface roughness (RMS = 2.51), and there is no Si diffusion in the ferroelectric film as the $La_2O_2CO_3$ also acts as a diffusion barrier. The evaluation of the EO properties results in a large r_{eff} of 138.68 $\mp$ 5.78 pm V^{-1}. Finally, the $BaTiO_3$ film is integrated into a SiN ring resonator and has a $V_\pi L$ of 1.881 $\mp$ 0.078 V cm and an EO bandwidth of 43 GHz. Consequently, we have developed a solution-based integration process for $BaTiO_3$ thin films using a $La_2O_2CO_3$ template film, which is a valuable alternative to the conventional processing method. In this way, low-cost, high-throughput and flexible integration of $BaTiO_3$ films on PIC platforms is possible, providing an opportunity to bridge the gap to large-scale integration of $BaTiO_3$ thin films on PIC platforms in the future.

4 Experimental

4.1 $BaTiO_3$ film fabrication

First, the substrates (Si, Si/SiO_2, Si/SiN, CG and CG/ITO) were successively ultrasonically cleaned with acetone, isopropanol and distilled water for 5 minutes and then heated on a hotplate at 120 °C in ambient atmosphere to remove solvent residues. A two-step manufacturing process is introduced for the production of the crystalline $BaTiO_3$ film. First, a $La_2O_2CO_3$ template film is fabricated and then the ferroelectric $BaTiO_3$ film is integrated. Both films are deposited using a CSD process. The formulation of the precursor solution and the deposition process of the $La_2O_2CO_3$ template film (7 nm) have already been reported elsewhere.[33] For the integration of the $BaTiO_3$ film, a precursor solution is formulated in which barium acetate (Alfa Aesar, 99%) and titanium butoxide (Merck, 97%) are dissolved together with additives in 1-butanol (Merck, $\geq$ 99%). A final molarity of 0.4 M was achieved and the ink was filtered with a 0.2 μm PET filter before deposition.[48] The $BaTiO_3$ precursor solution was spincoated on the $La_2O_2CO_3$ film at a spin speed of 3000 rpm for 30 s using a KLM SCC-200 model. Finally, the wet $BaTiO_3$ film was pyrolyzed at 200 °C for 10 min in ambient atmosphere and then annealed in a Jipelec jetfirst 150 rapid thermal annealing (RTA) furnace under static air at an annealing temperature of 750 °C to obtain a highly crystalline $BaTiO_3$ film.[62]

4.2 Phase composition, texture and surface characterization

Phase composition and texture of the $BaTiO_3$ thin film were characterized by GIWAXS, θ-2θ XRD measurements, pole figures and HRTEM. The GIWAXS data was obtained at NCD-SWEET beamline at the ALBA Synchrotron Radiation Facility (Spain). The incident X-ray beam energy was set to 12.4 keV (λ = 0.9998 Å) using a channel cut Si (111) monochromator. An array of Be lenses (total of 6), also known as Be Compound Refractive Lenses (CRLs), were used to collimate the beam, resulting in a beam size of 50 × 150 μm^2 (V × H) at the sample position. The angle of incidence α_i was screened between 0° and 1° and finally set at 0.325° ensuring surface sensitivity. An exposure time of 10 s was used. The scattering patterns were recorded using a Rayonix LX255-HS area detector, which consists of a array of 1920 × 5760 pixels (H × V) with a pixel size of 44.27 × 44.27 μm^2. The scattering vector |q| was calibrated using Cr_2O_3 as a standard sample, obtaining a sample-to-detector distance of 201.65 mm. The intrinsic 2D GIWAXS pattern is corrected as a function of the components of the scattering vector and was reported here after integration and conversion of the scattering vector (q) to 2θ. The θ-2θ XRD measurements were performed on a Bruker D8 Advance diffractometer (Cu-Kα λ = 1.54184 Å) equiped with a LynxEye XE-T Silicon strip line detector. The diffraction was measured between 2θ = 20° and 50° with a step width of 0.02°, step time of 4 s and an additional Ni filter. Subsequently, a LF is calculated from the XRD intensities (20° - 70°), and is defined as the following equation: $LF = (p-p_0)/(1-p_0)$. Where p denotes the fraction of the summation of the peak intensities corresponding to the preferred orientation axis to that of the summation of all diffraction peaks in particle-oriented materials. p_0 is p of the material with a random particle distribution. The LF varies between 0 and 1, LF = 0 corresponds to random orientation, and LF = 1 to perfect orientation.[63] Additional textural experiments on samples with different thicknesses were performed on the XMaS-BM28 beamline, the EPSRC-funded UK-CRG at the European Synchrotron Radiation Facility (France).[64] A Dectris - Pilatus3 300k detector (487 × 619 pixels, pixel size 0.172 × 0.172 mm^2) was used to collect the (002) and (200) $BaTiO_3$ reflections. The detector was placed at 1.1 m from the sample. The beam energy was set at 12.4 keV (λ = 0.1 nm). To find the out-of-plane reflection, the sample-detector is positioned in Bragg conditions, with an incident angle θ=13.3° and the detector at an exit angle 2θ = 28.7° in vertical. To collect the in-plane reflection, we used grazing-incidence conditions: with a shallow incident angle θ=0.24° and the detector at an exit angle 2θ = 28.7° along the horizontal plane. Several frames were taken and then averaged. We used 1 s of exposure time for every frame. Pole figure measurements of the film were determined using a Panalytical Empyrean XRD with Cu K_α radiation, Bragg-Brentano HD beam conditioning, five-axis goniometer and PixCel3D detector. HRTEM images were acquired on a JEOL JEM-2200FS TEM at Ghent University TEM core facility operated at 200 kV and equipped with Cs corrector. For the TEM measurements, a cross-sectional TEM lamella was prepared using *in situ* lift out procedure on the FEI Nova 600 Nanolab Dual Beam focused ion beam (FIB) SEM. The composition of the thin film was measured by XPS depth profiling on an S-probe XPS spectrometer with monochromatic Al radiation (1486.6 eV). Ar^+ ion sputtering (4 keV), on a sputtering area of 3 ×3 mm^2, was carried-out in consecutive sputter cycles of 50s. The argon pressure was controlled with a thermo valve. In each cycle, atoms were removed from the surface, and a quantitative analysis on an area of 250 × 1000 μm^2 of the fresh surface was performed. The intensities of the Ba ($3d_{5/2}$), La ($3d_{5/2}$), Ti (2p), Si (2s), C (1s) and O (1s) peaks were measured with a pass energy of 90 eV and an energy step of 0.1 eV, The flood gun was set at 3 eV. A nickel grid was placed 3 mm above the samples in order to suppress charging of the samples. The relative atomic concentrations were estimated using the software package CasaXPS (Casa Software Ltd., UK) using a Shirley background and Scoffield sensitivity factors. The surface microstructure of the $BaTiO_3$ films was analyzed by SEM using a JEOL FEG SEM JSM-7600F at an accelerating voltage of 10 kV. The surface roughness of the film was determined by AFM using a Bruker Dimension Edge system in tapping mode in air. The RMS of the roughness values was calculated using 3 μm × 3 μm micrographs.

4.3 Electro-optic characterization

In order to quantify the EO effect, measurements were performed in free space using a similar setup as described in the work of Abel et al.[23] An r_{eff} was calculated by determining the electric field-induced polarization change of a transmitted laser beam (generated using a 1550 nm fiber coupled laser diode). An interdigitated electrode pattern is defined on the sample using UV-lithography, Ti/Au e-gun deposition and lift-off. Here, the desired electrode pattern is embedded into the photoresist using a Karl Suss MA6 Mask Aligner. A 10 nm titanium film and 400 nm Au film is deposited using a Leybold UNIVEX coating system and lift-off is used to remove regions of unexposed resist. The initial Ti film acts as an adhesive film between the Au and the substrate. Linearly polarized light passes through the $BaTiO_3$ film under perpendicular incidence with a polarization direction of 45° with respect to the electrodes. The laser light is first collimated using an aspheric collimator lens and then focused between the electrode with a gap of 10 μm using another aspheric lens. The refractive index change in the $BaTiO_3$ film due to the applied electric film causes birefringence of the incident light. After passing through a half-wave plate and polarizer, the transmitted power is proportional to the induced retardation. A modulated signal of $V_{mod} = 5$V at a frequency of $f = 25$ kHz was used and the EO response was amplified through a lock-in detection scheme. A schematic representation of the measurement setup can be found in Figure S6. In this setup, the transmitted optical power P_{out} is given by (see SI, equation (S7)):

$$P_{out} = \left(\frac{1}{2} + \frac{\alpha\pi n^3 r_{eff} V_{mod} t}{2\lambda g}\right) P_{in} \tag{6}$$

Where λ is the wavelength of the laser, g is the distance between the electrodes, α a correction factor for the electric field,[52] n is the refractive index and t is the thickness of the $BaTiO_3$ film, V_{mod} is the amplitude of the modulated signal, P_{in} is the incident laser power and r_{eff} the effective Pockels coefficient. The refractive index was calculated with a reflectometry set-up using the QE Pro series spectrometer. The correction factor α is used to correct the parallel plate capacitor approximation where $E = V/g$. α is calculated using a finite elements solver and defined such that $E = \alpha V/g$. From the aforementioned equation, it is possible to determine the r_{eff} of the $BaTiO_3$ thin film. In contrast to the previously reported free-space measurements of epitaxial ferroelectric $BaTiO_3$ films, it is not needed here to align the electric field with respect to an in-plane crystal axis (e.g. [011]) of the $BaTiO_3$ film since the polarization of the domains is randomly oriented in-plane due to the fiber texture of the $BaTiO_3$ film.[23, 55, 25] Consequently, the EO response of the fiber textured $BaTiO_3$ film is not dependent on the in-plane orientation of the electrode on the sample. Finally, stability over time of the $BaTiO_3$ thin film was investigated by applying a constant DC bias voltage over 40 hours while measurements were taken each minute to calculate the r_{eff}.

4.4 Device fabrication and characterization

In this work, silicon-nitride (SiN) PICs are used for two main reasons. First, SiN waveguides could be integrated directly on the $BaTiO_3$ film which minimizes the processing steps. Second, the low refractive index of SiN results in a high optical power confinement in the $BaTiO_3$ film resulting in a high mode overlap. The simulation results of the design are shown in Figure S7 and S8. A 120 nm crystalline $BaTiO_3$ film was deposited as described earlier on a Si/SiO_2 (3 μm) substrate. A 150 nm thick SiN layer was then deposited on top of the $BaTiO_3$ film using an Advanced Vacuum Vision 310 plasma enhanced chemical vapour deposition (PECVD) system. After deposition, a Raith Voyager Electron Beam Lithography (EBL) system was used to pattern the designs. The designs were then etched into the SiN layer using an Advanced Vacuum Vision 320 reactive ion etcher (RIE). Finally, electrode patterns were defined on the sample using UV-lithography, Ti/Au e-gun deposition and lift-off. A graphical representation of the device cross-section is shown in Figure S9. The DC operation of the $BaTiO_3$ film was investigated using a SiN O-band ring resonator with a simple benchtop measurement setup. A tunable TSL-510 O-band laser from Santec was used to generate light at a wavelength of 1310 nm. As our in-house PECVD SiN waveguides have lower transmission losses at this wavelength than at 1550 nm wavelength. This light was cou-

pled into and out of the photonic chip via grating couplers specifically designed for this film stack and wavelength (Figure S10 and S11). The transmitted light was recorded using a Newport 1936-R optical power meter. A Keithley 2400 Standard Series source measure unit (SMU) and MPI coaxial DC probes were used to contact and apply voltages to the gold electrodes on the ring resonator. High-speed operation of fabricated SiN-O-band ring resonator was investigated using an Agilent PNA-X N5247A network analyzer. This network analyzer serves as both source and receiver for the electrically modulated signal. The same tunable O-band laser Santec TSL-510 was used to generate light with a wavelength of 1310 nm. Ground-signal GS-50A RF probes were used to make the electrical contacts between the network analyzer and the ring resonator electrodes, and the output is measured with a Finisar XPDV3120 70-GHz photodetector, which is coupled back into the network analyzer to extract the full network scattering matrix. A diagram of this setup is shown in Figure S12.

Supporting Information
Supporting Information is available from the Wiley Online Library or from the author.

Conflict of Interest
The authors declare no conflict of interest.

Acknowledgements
The authors thank Laura Van Bossele and Els Bruneel for performing the XRD (θ-2θ) and XPS measurements, respectively. GIWAXS experiments were performed at NCD-SWEET beamline at ALBA Synchrotron with the collaboration of ALBA staff. TEM measurements were performed by Hannes Rijckaert at the UGent TEM Core Facility. Ewout Picavet gratefully acknowledges the support and funding as SB-PhD Fellow of the Research Foundation Flanders (FWO, grant number 3S041219). Hannes Rijckaert gratefully acknowledges the support and funding as a postdoctoral fellow fundamental research by the Research Foundation Flanders (FWO, grant number 1273621N). Petriina Paturi acknowledges the Jenny and Antti Wihuri Foundation for financial support. This work was financially supported by the Special Research Fund - UGent (BOF20/GOA/027).

References

[1] C. Soci, G. Adamo, D. Cortecchia, K. Wang, S. Xiao, Q. Song, A. L. Schall-Giesecke, P. J. Cegielski, M. C. Lemme, D. Gerace, et al., *Optical Materials: X* **2023**, *17* 100214.

[2] D.-S. Liu, J. Wu, H. Xu, Z. Wang, *Advanced Materials* **2021**, *33*, 4 2003733.

[3] K. Wang, G. Xing, Q. Song, S. Xiao, *Advanced Materials* **2021**, *33*, 6 2000306.

[4] E. L. Wooten, K. M. Kissa, A. Yi-Yan, E. J. Murphy, D. A. Lafaw, P. F. Hallemeier, D. Maack, D. V. Attanasio, D. J. Fritz, G. J. McBrien, et al., *IEEE Journal of selected topics in Quantum Electronics* **2000**, *6*, 1 69.

[5] T. Vanackere, T. Vandekerckhove, L. Bogaert, M. Billet, S. Poelman, S. Cuyvers, J. Van Kerrebrouck, A. Moerman, O. Caytan, N. Singh, et al., *APL Photonics* **2023**, *8*, 8.

[6] K. Alexander, J. P. George, J. Verbist, K. Neyts, B. Kuyken, D. Van Thourhout, J. Beeckman, *Nature communications* **2018**, *9*, 1 1.

[7] G. F. Feutmba, L. Da Silva, N. Singh, L. Breyne, K. De Geest, J. P. George, J. Bauwelinck, D. Van Thourhout, X. Yin, J. Beeckman, *Optical Materials Express* **2023**, *13*, 7 2120.

[8] T. Jin, P. T. Lin, *IEEE journal of selected topics in quantum electronics* **2020**, *26*, 5 1.

[9] F. Eltes, C. Mai, D. Caimi, M. Kroh, Y. Popoff, G. Winzer, D. Petousi, S. Lischke, J. E. Ortmann, L. Czornomaz, et al., *Journal of Lightwave Technology* **2019**, *37*, 5 1456.

[10] F. Eltes, M. Kroh, D. Caimi, C. Mai, Y. Popoff, G. Winzer, D. Petousi, S. Lischke, J. E. Ortmann, L. Czornomaz, et al., In *2017 IEEE International Electron Devices Meeting (IEDM)*. IEEE, **2017** 24–5.

[11] M. Zhu, Z. Du, S. S. Chng, S. H. Tsang, E. H. T. Teo, *Journal of Materials Chemistry C* **2018**, *6*, 47 12919.

[12] W. Guo, A. B. Posadas, A. A. Demkov, *Journal of Vacuum Science & Technology A* **2021**, *39*, 3.

[13] F. Eltes, D. Caimi, F. Fallegger, M. Sousa, E. O'Connor, M. D. Rossell, B. Offrein, J. Fompeyrine, S. Abel, *Acs Photonics* **2016**, *3*, 9 1698.

[14] P. Girouard, P. Chen, Y. K. Jeong, Z. Liu, S.-T. Ho, B. W. Wessels, *IEEE Journal of Quantum Electronics* **2017**, *53*, 4 1.

[15] S. Abel, F. Eltes, J. E. Ortmann, A. Messner, P. Castera, T. Wagner, D. Urbonas, A. Rosa, A. M. Gutierrez, D. Tulli, et al., *Nature materials* **2019**, *18*, 1 42.

[16] J. E. Ortmann, F. Eltes, D. Caimi, N. Meier, A. A. Demkov, L. Czornomaz, J. Fompeyrine, S. Abel, *ACS Photonics* **2019**, *6*, 11 2677.

[17] P. Bernasconi, M. Zgonik, P. Günter, *Journal of applied physics* **1995**, *78*, 4 2651.

[18] R. A. McKee, F. Walker, M. Chisholm, *Physical Review Letters* **1998**, *81*, 14 3014.

[19] D. Diaz-Fernandez, M. Spreitzer, T. Parkelj, D. Suvorov, *Applied Surface Science* **2018**, *455* 227.

[20] Z. Wang, B. Goodge, D. Baek, M. Zachman, X. Huang, X. Bai, C. Brooks, H. Paik, A. Mei, J. Brock, et al., *Physical Review Materials* **2019**, *3*, 7 073403.

[21] H. E. Swanson, *Standard X-ray diffraction powder patterns*, volume 25, US Department of Commerce, National Bureau of Standards, **1953**.

[22] V. M. Longo, M. d. G. S. Costa, A. Z. Simoes, I. L. V. Rosa, C. O. P. Santos, J. Andres, E. Longo, J. A. Varela, *Physical Chemistry Chemical Physics* **2010**, *12*, 27 7566.

[23] S. Abel, T. Stöferle, C. Marchiori, C. Rossel, M. D. Rossell, R. Erni, D. Caimi, M. Sousa, A. Chelnokov, B. J. Offrein, et al., *Nature communications* **2013**, *4*, 1 1671.

[24] K. J. Kormondy, Y. Popoff, M. Sousa, F. Eltes, D. Caimi, M. D. Rossell, M. Fiebig, P. Hoffmann, C. Marchiori, M. Reinke, et al., *Nanotechnology* **2017**, *28*, 7 075706.

[25] A. B. Posadas, H. Park, M. Reynaud, W. Cao, J. D. Reynolds, W. Guo, V. Jeyaselvan, I. Beskin, G. Z. Mashanovich, J. H. Warner, et al., *ACS Applied Materials & Interfaces* **2021**, *13*, 43 51230.

[26] T.-H. Wang, P.-C. B. Hsu, M. Korytov, J. Genoe, C. Merckling, *Journal of Applied Physics* **2020**, *128*, 10.

[27] B. Wagué, G. Niu, G. Dong, L. Dai, P. Roy, G. Saint-Girons, P. Rojo-Romeo, Y. Robach, B. Vilquin, et al., *Thin Solid Films* **2020**, *693* 137636.

[28] A. Karvounis, F. Timpu, V. V. Vogler-Neuling, R. Savo, R. Grange, *Advanced Optical Materials* **2020**, *8*, 24 2001249.

[29] J. Winiger, K. Keller, P. Gjini, D. Moor, M. Baumann, D. Chelladurai, M. Kohli, R. Schwanninger, Y. Fedoryshyn, C. Tommaso, et al., *Optics Express* **2024**, *32*, 3 4511.

[30] S. Hirano, S. Shimada, M. Kuwabara, *Applied Physics A* **2005**, *80* 783.

[31] Ü.-L. Talts, H. C. Weigand, G. Saerens, P. Benedek, J. Winiger, V. Wood, J. Leuthold, V. Vogler-Neuling, R. Grange, *Small* **2023**, *19*, 50 2304355.

[32] F. Timpu, M. Reig Escalé, M. Timofeeva, N. Strkalj, M. Trassin, M. Fiebig, R. Grange, *Advanced Optical Materials* **2019**, *7*, 22 1900936.

[33] E. Picavet, H. Rijckaert, E. Solano, O. Bikondoa, E. G. Fernandez, P. Paturi, L. Van Bossele, H. Vrielinck, J. Beeckman, K. De Buysser, *Journal of Materials Chemistry C* **2023**, *11*, 23 7705.

[34] Z. V. Ooi, A. A. Saif, Y. Wahab, Z. A. Z. Jamal, *AIP Conference Proceedings* **2017**, *1835*, 1.

[35] K. He, N. Chen, C. Wang, L. Wei, J. Chen, *Crystal Research and Technology* **2018**, *53*, 2 1700157.

[36] K. J. Kormondy, S. Abel, F. Fallegger, Y. Popoff, P. Ponath, A. B. Posadas, M. Sousa, D. Caimi, H. Siegwart, E. Uccelli, et al., *Microelectronic Engineering* **2015**, *147* 215.

[37] W. Lu, D.-N. Fang, C. Li, K.-C. Hwang, *Acta Materialia* **1999**, *47*, 10 2913.

[38] F. Li, R. Rajapakse, *Acta Materialia* **2007**, *55*, 19 6472.

[39] J. Schultheiß, L. Liu, H. Kungl, M. Weber, L. K. Venkataraman, S. Checchia, D. Damjanovic, J. E. Daniels, J. Koruza, *Acta materialia* **2018**, *157* 355.

[40] W. Li, C. M. Landis, A. A. Demkov, *Physical Review Materials* **2022**, *6*, 9 095203.

[41] M. G. Norton, C. Scarfone, J. Li, C. B. Carter, J. W. Mayer, *Journal of materials research* **1991**, *6*, 10 2022.

[42] L. Bendersky, C. Lu, J. Scott, K. Chang, I. Takeuchi, *Journal of materials research* **2002**, *17*, 10 2499.

[43] D. J. Appleby, N. K. Ponon, K. S. Kwa, S. Ganti, U. Hannemann, P. K. Petrov, N. M. Alford, A. O'Neill, *Journal of Applied Physics* **2014**, *116*, 12.

[44] I. Spasojevic, G. Sauthier, J. M. Caicedo, A. Verdaguer, N. Domingo, *Applied Surface Science* **2021**, *565* 150288.

[45] N. Domingo, E. Pach, K. Cordero-Edwards, V. Pérez-Dieste, C. Escudero, A. Verdaguer, *Physical Chemistry Chemical Physics* **2019**, *21*, 9 4920.

[46] D. Fork, F. Armani-Leplingard, J. Kingston, G. Anderson, *MRS Online Proceedings Library (OPL)* **1995**, *392* 189.

[47] K. Bakken, A. B. Blichfeld, I.-E. Nylund, D. Chernyshov, J. Glaum, T. Grande, M.-A. Einarsrud, *Chemistry-Methods* **2022**, *2*, 2 e202100064.

[48] J. P. George, J. Beeckman, W. Woestenborghs, P. F. Smet, W. Bogaerts, K. Neyts, *Nanoscale research letters* **2013**, *8* 1.

[49] F. Leroy, A. Rousseau, S. Payan, E. Dogheche, D. Jenkins, D. Decoster, M. Maglione, *Optics Letters* **2013**, *38*, 7 1037.

[50] S. Sharma, A. Paliwal, M. Tomar, F. Singh, N. K. Puri, V. Gupta, *Journal of materials science* **2016**, *51* 4055.

[51] B. I. Edmondson, S. Kwon, C. H. Lam, J. E. Ortmann, A. A. Demkov, M. J. Kim, J. G. Ekerdt, *Journal of the American Ceramic Society* **2020**, *103*, 2 1209.

[52] T. Van de Veire, J. George, H. Rijckaert, K. Neyts, J. Lauwaert, F. Beunis, J. Beeckman, *Journal of Applied Physics* **2021**, *129*, 9.

[53] P. Mirzadeh Vaghefi, A. Baghizadeh, A. A. Lourenço, V. S. Amaral, A. L. Kholkin, *Materials* **2017**, *10*, 9 1107.

[54] K. M. Rabe, C. H. Ahn, J.-M. Triscone, *Physics of ferroelectrics: a modern perspective*, volume 105, Springer Science & Business Media, **2007**.

[55] B. I. Edmondson, S. Kwon, J. E. Ortmann, A. A. Demkov, M. J. Kim, J. G. Ekerdt, *Journal of the American Ceramic Society* **2020**, *103*, 10 5700.

[56] A. T. Vasudevan, S. K. Selvaraja, *Optical Materials Express* **2023**, *13*, 4 956.

[57] J. Nordlander, F. Eltes, M. Reynaud, J. Nürnberg, G. De Luca, D. Caimi, A. A. Demkov, S. Abel, M. Fiebig, J. Fompeyrine, et al., *Physical Review Materials* **2020**, *4*, 3 034406.

[58] S. Vura, V. Jeyaselvan, R. Biswas, V. Raghunathan, S. K. Selvaraja, S. Raghavan, *ACS Applied Electronic Materials* **2021**, *3*, 2 687.

[59] P. Gunter, *Applied Optics* **1988**, *27*, 12 2385.

[60] M. He, M. Xu, Y. Ren, J. Jian, Z. Ruan, Y. Xu, S. Gao, S. Sun, X. Wen, L. Zhou, et al., *Nature Photonics* **2019**, *13*, 5 359.

[61] F. Valdez, V. Mere, S. Mookherjea, *Optica* **2023**, *10*, 5 578.

[62] K. Bakken, A. B. Blichfeld, D. Chernyshov, T. Grande, J. Glaum, M.-A. Einarsrud, *Journal of Sol-Gel Science and Technology* **2020**, *95* 562.

[63] R. Furushima, S. Tanaka, Z. Kato, K. Uematsu, *Journal of the Ceramic Society of Japan* **2010**, *118*, 1382 921.

[64] O. Bikondoa, L. Bouchenoire, S. D. Brown, P. B. Thompson, D. Wermeille, C. A. Lucas, M. Cooper, T. P. Hase, *Philosophical Transactions of the Royal Society A: Mathematical, Physical and Engineering Sciences* **2019**, *377*.

Table of Contents

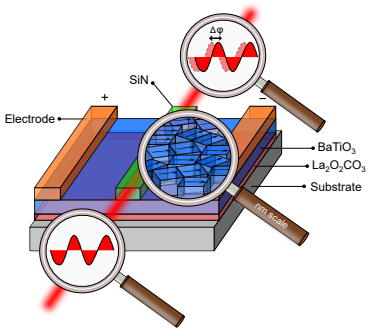

Here, an alternative method is proposed for the integration of highly textured $BaTiO_3$ films using a $La_2O_2CO_3$ template film in combination with a chemical solution deposition (CSD) process. This process route enables the cost-effective, high-throughput and flexible processing of high-quality heterogeneously integrated $BaTiO_3$ phase modulators.